

Design of active materials distributions for four-dimensional printing based on multi-material topology optimization

Yawen Wei¹, Pei Huang^{1,2}, Zhen Li¹, Pengfei Wang^{1,*} and Xiangchao Feng^{1,*}

¹ Qian Xuesen Laboratory of Space Technology, China Academy of Space Technology, Beijing 100094, China

² School of Energy and Power Engineering, Nanjing University of Science and Technology, Nanjing 210094, China

E-mail: wangpengfei@qxslab.cn , fengxiangchao@qxslab.cn

Received xxxxxx
Accepted for publication xxxxxx
Published xxxxxx

Abstract

Printed active composites (PACs) are capable of deforming from an initial shape to a target shape via spatial arrangements of active materials within a passive matrix. Multi-material polymer printers allow precise placement of multiple materials in the design space. However, Single active material is difficult to satisfy the demand in the high-precision matching of more complex target shape. Hence, a multi-material topology optimization approach for the design of PACs is proposed to achieve a target shape under a given stimulus. A multi-material interpolation function for active materials is established, and continuum mechanics modeling is used for simulating active material behaviors on a voxel basis to compute deformations for a given material distribution. The adjoint method is used for sensitivity analysis. Numerical simulations, of different target shapes with the same initial shape, verify the effectiveness of the method. The proposed method is feasible in the conceptual designs of PAC material distributions benefit with stable convergence, ease of implementation, and low computational costs.

Keywords: topology optimization, multi-material, printed active composites, 4D printing

1. Introduction

Printed active composites (PACs) are composed of active materials and a non-active matrix. The non-active matrix (passive material) is usually compliant. The active materials, which are environmentally responsive, mainly category into shape-memory polymers [1][2], dielectric elastomers [3], and liquid-crystal elastomers [4][5]. Various stimuli are used to drive active materials, such as temperature [6][7], pH [8], humidity [9], magnetic fields [10][11], and electric fields

[12]. PACs can evolve in a predetermined manner over time, which is referred to four-dimensional (4D) printing [13][14]. The final shape of the PAC is a result of interactions between the active and passive phases and environmental stimulus [15]. Therefore, the shape evolution is dependent on the spatial arrangement of the active and passive phases. This gives a PAC a huge advantage because, by designing the arrangement of the active and passive phases in a structure, it can deform into the target shape upon external stimulus. Furthermore, advanced three-dimensional (3D) printers have

the ability to precisely place multiple materials in the design space [7][16][17].

For a given target shape, it is difficult to find the optimal spatial distribution of constituent materials because the design process is a challenging inverse problem with a particular geometry and boundary-value problem [18]. Previous approaches for active composite design may be classified into analytical methods and optimization algorithms. Analytical methods derive the corresponding material properties of each design element through a series of equations for the target shape. For example, an analytical method, for the design of shape-shifting structured lattices, computes the required growth and curvatures of the lattice ribs from the conformal projection of the target shape [7]. Optimization algorithms are mostly adopted in the design of general structures for active composites. Depending on whether gradient information is used, the algorithms can be roughly divided into evolutionary algorithms and topology optimization methods. The main advantages of evolutionary algorithms are that they do not require gradient calculations of the objective functions, and they allow parallelization. For example, to prevent a whole wing from stalling at the same time, Sossou et al. [19] used a slightly twisted wing as a target shape and used a genetic algorithm to calculate the spatial distribution of a hard silicone and two hypothetically magnetostrictive composite materials in the initial shape. Similarly, machine learning was proposed for the design of active composite structures that can achieve target-shape-shifting responses [18]. However, evolutionary algorithms are hindered by several factors. The first is that finer voxelization is required when a complex target shape or high-precision shape-matching is considered. The finer voxelization requires the implementation of large-scale population in evolutionary algorithms which involves extensive computational costs and a difficult convergence. The second shortcoming is that filtering of the material distribution was not considered in the above cases, further resulting in checkerboard patterns and the islanding phenomenon. These cause undulations in the material distributions and affect shape-matching and structural performance. For example, wing-surface undulations are likely to reduce the airworthiness of a plane [19].

Topology optimization is a powerful conceptual design method that has been widely adopted in both academic research and industrial applications [20]. It is used to find the best material distribution in a design domain that maximizes the specific performance of the structure. Many topology optimization methods have been developed, including the solid isotropic material with penalization (SIMP) method [20][21], the level-set method [22], the evolutionary structural optimization method [23][24], the moving morphable components method [25][26], as well as other methods [27–31]. Topology optimization has also been used

in PAC layout designs for 4D printing. For example, the level-set method has been used to determine the distribution of shape-memory polymers within a passive matrix. In this way, active composites are deformed from an initial shape into a target shape under thermal actuation [15][32]. Applying the SIMP method in the structural design for 4D printing resulted in high-performance porous soft actuators [33][34]. In addition, SIMP has been used to calculate the spatial arrangement of soft and relatively hard materials in a soft gripper for maximum bending deflections [35]. Most of the aforementioned target-shape-matching cases focused on the spatial arrangements of a passive material and a single active material. However, under external stimuli, the deformability of the active material is affected by its Young's modulus and the material properties related to the stimulus response behavior, such as thermal expansion coefficient, piezoelectric coefficient, etc. Therefore, as a more complex target shape is considered, a single active material is not sufficient for high-precision matching of the target shape.

To address the above issues, multi-material topology optimization for PAC design is proposed to solve the spatial arrangement of multiple active materials and a passive material for a given target shape. More specifically, a multi-material interpolation equation for active materials was used to model the material distribution in terms of continuous variables. The voxel vertices displacement field error of the achieved shape, relative to the target shape, that corresponds to the design variables was defined as an objective function. The Zhang–Paulino–Ramos (ZPR) design-variable update scheme was adopted to solve the topology optimization problem where the volume constraints of each active material are considered.

The remainder of this paper is organized as follows. Material modeling and deformation computation is introduced in Section 2. In section 3, the multi-material topology optimization formulation for 4D printing design is provided. Subsequently, the results of several examples are illustrated to demonstrate the efficiency of the proposed method in section 4. Finally, a discussion of the results and some concluding remarks are presented.

2. Material modeling and Deformation computation

2.1 Material modeling

To accurately model the responses of PACs, geometric nonlinearities and complex thermomechanical constitutive behaviors need to be considered, leading to a nonlinear, non-conservative multi-physical model [15]. During topology optimization, the objective function must be repeatedly called to calculate the structural displacement. Consideration of these models within the conceptual design phase significantly increases the algorithmic complexity and the computational cost. To mimic the behavior of the active

material with computational speed and an easy implementation with suitable fidelity, a continuum mechanics model for simulating the active and passive material behaviors in a voxel basis [36] was adopted. The modeled active materials were limited to non-programmable shape-changing active materials, such as piezoelectric materials, electro-, magneto-, or photo-strictive materials, and hydrogels. A detailed discussion of the modeling scheme for these active materials was reported in Ref. [36].

The two-dimensional (2D) design domain is shown in **Figure 1**, in which the approach for modeling material behavior is organized in four steps: (1) Discretize the design domain into equally sized voxelized object. (2) Extract the control structure of design domain by using beams to connect voxels' centers. (3) Calculate the deformation of the control structure. (4) Calculate the deformation of voxelized object. Step (3) and (4) are described in detail in the subsequent section 2.2.

Each voxel is assumed to be homogeneous and made of a single linear and isotropic material. And each voxel can represent different active materials and passive material. In the 2D design domain, the Deformability of the active material is affected by the Young's modulus E and the deformation coefficient g . The deformation coefficient g is determined by the material parameters related to the stimulus response behavior and the environmental stimulus, which is used to characterize the deformation ability of the material under a given stimulus. Beams materials properties are inherited from the pairs of voxels they are connecting, as described by Eq.(1):

$$\hat{E}_e = \frac{2E_{e1}E_{e2}}{E_{e1} + E_{e2}}, \hat{g}_e = \frac{2g_{e1}g_{e2}}{g_{e1} + g_{e2}} \quad (1)$$

where $e1$ and $e2$ are the number index of the pairs of voxels corresponding to the e^{th} beam element.

2.2 Deformation computation

The direct stiffness method [37] is employed for computing the deformation of the control structure. Each node has three degrees of freedoms (DOFs) in two-dimensions. A beam's stiffness matrix in a local coordinate system is written as:

$$\bar{\mathbf{k}}_e = \begin{bmatrix} \frac{EA}{L} & 0 & 0 & -\frac{EA}{L} & 0 & 0 \\ 0 & \frac{12EI}{L^3} & \frac{6EI}{L^2} & 0 & -\frac{12EI}{L^3} & \frac{6EI}{L^2} \\ 0 & \frac{6EI}{L^2} & \frac{4EI}{L} & 0 & -\frac{6EI}{L^2} & \frac{2EI}{L} \\ -\frac{EA}{L} & 0 & 0 & \frac{EA}{L} & 0 & 0 \\ 0 & -\frac{12EI}{L^3} & -\frac{6EI}{L^2} & 0 & \frac{12EI}{L^3} & -\frac{6EI}{L^2} \\ 0 & \frac{6EI}{L^2} & \frac{2EI}{L} & 0 & -\frac{6EI}{L^2} & \frac{4EI}{L} \end{bmatrix} \quad (2)$$

where L is the voxel size. $A = L^2$ is the beam cross section area. $I = \frac{L^4}{12}$ is the beam moments of inertia.

The active response behavior of the active material is modeled by the initial force vector $\bar{f}_e(\mathbf{S})$ in Eq.(3). The magnitude of the element internal force vector is affected by Young's modulus E_e and deformation coefficient g_e of the element. Eq.(3) and Eq.(4) are both written in a local coordinate system. In order to calculate the displacement of the nodes, they need to be converted to a global coordinate system.

$$\bar{k}_e \bar{u}_e = \bar{f}_e^M + \bar{f}_e(\mathbf{S}) \quad (3)$$

$$\bar{f}_e(\mathbf{S}) = E_e A g_e (\mathbf{a}, \mathbf{S}) [-1 \ 0 \ 0 \ 1 \ 0 \ 0]^T \quad (4)$$

where \bar{f}_e^M is the external force vector. \mathbf{S} denotes the

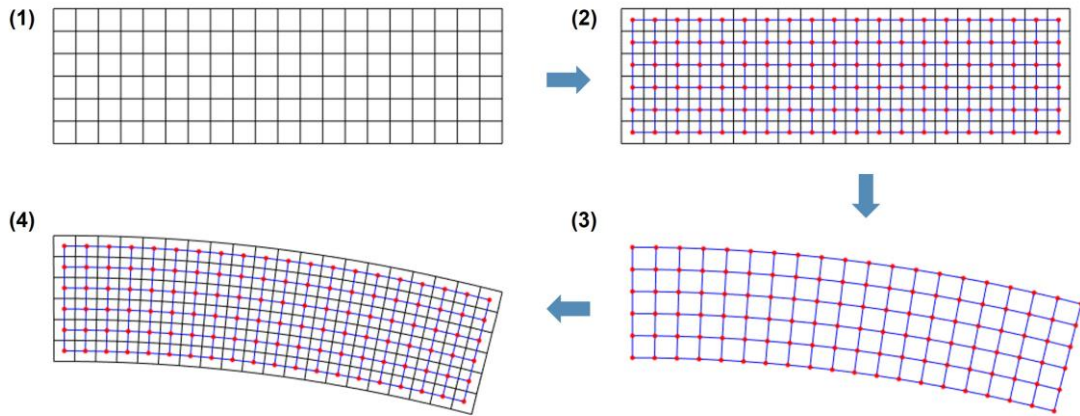


Figure 1. Continuum mechanics modeling scheme

stimulus. α denotes a vector containing all the active materials properties related to its stimulus responsive behavior.

According to the deformation map associated with each beam, each beam has an influence zone which is occupied by the two voxels that the beam is connecting. Each voxel has 4 vertices (its corners). The vertices belonging to the zone are influenced by the beam deformation. A vertex affected by many influence zones is calculated by using a weighted average deformation map. Assuming that the vertex is

affected by N beams, then the weight is given by $w_i = \frac{1}{N}$.

Therefore, the deformation of all voxel vertices can be obtained by the deformation of the control structure [36][38].

The advantage of the continuum mechanics modeling scheme is to quickly obtain the active response behavior of a given material distribution with only a little loss of accuracy. Compared with finite element method (FEM) simulations, the continuum mechanics modeling scheme for conceptual design is not accurate enough. However, the error of the two methods will gradually decrease as voxel size decreases. Here a case is used to illustrate this rule.

As illustrated in **Figure 2**, a cantilever beam ($L=30$ mm, $H=10$ mm) is defined with its left end set with fixed boundary conditions. The upper and lower parts of the cantilever beam are made of two materials. The properties of the two material are summarized in **Table 1**. The cantilever beam bends downwards with a temperature change of $\Delta T = 200$ °C, and the maximum displacement is 3.39 mm.

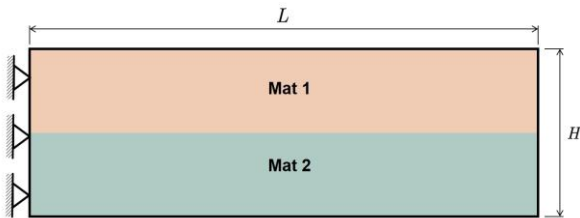


Figure 2. The bi-material cantilever beam: boundary conditions and material distribution

Table 1. Material properties of the bi-material cantilever beam

Property	Mat 1	Mat 2
Young's modulus (MPa)	10	5
Coefficient of thermal expansion ($10^{-6} / ^\circ\text{C}$)	260	10

To examine the effect of voxel size on the accuracy, four meshes with different element number are generated, as shown in **Figure 3**. The mesh is both a FEM mesh and a voxel mesh. So, the nodes of the finite element are the vertices of the voxels.

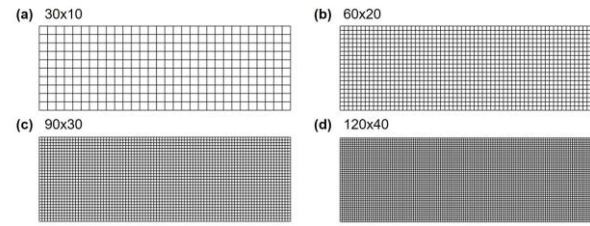


Figure 3. Four meshes with different voxel size (a) 30×10 (b) 60×20 (c) 90×30 (d) 120×40

The finite element analysis was run in ANSYS. The number of voxels on the width H ([10, 20, 30, 40]) corresponds to the voxel size ([1, 0.5, 0.33, 0.25] mm). The number of voxels on the width is taken as the horizontal axis, and the absolute value of the maximum node displacement error is taken as the vertical axis. As mesh density increases and voxel size decreases, the maximum node displacement error between the continuum mechanics modeling scheme and FEM results is also reduced shown in **Figure 4**. This accuracy is sufficient for conceptual design.

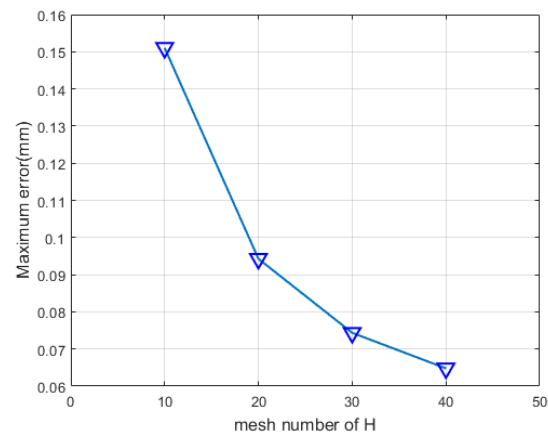


Figure 4. The maximum node displacement error results for different voxel size

3. Multi-material topology optimization for 4D printing design

3.1 Problem Definition

In the design problem of PAC in 4D printing, the final shape of PAC is determined by the initial shape, environmental stimuli and material distribution. It means that the shape change can be controlled by specifying the material distribution in the initial shape. As the complexity of the target shape increases, a single active material is difficult to achieve satisfy the demand in the high-precision matching of the target shape. It is of great significance to consider multiple active materials as candidate materials. Consequently, the purpose of this problem is to find the best material distribution subject to volume constraints to

minimize the error between the final shape and the target shape.

As discussed in section 2, the deformation of the voxelized object is driven by the deformation of the control structure. To reduce the complexity of sensitivity analysis, the beams' node displacement \mathbf{U} is used to describe the achieved shape. Similarly, the target beams' node displacement \mathbf{U}^* is used to describe the target shape. The discrete problem, for the design of PAC in 4D printing, accommodates many candidate materials and many volume constraints is expressed as:

$$\begin{aligned} \min \quad & J = \frac{(\mathbf{U} - \mathbf{U}^*)^T (\mathbf{U} - \mathbf{U}^*)}{N} \\ \text{s.t.} \quad & \mathbf{K}(\mathbf{z}) \mathbf{U}(\mathbf{z}) = \mathbf{F}(\mathbf{z}) \\ & \varphi_j = \frac{\sum_{i=1}^{N_c} \hat{z}_{ij}}{N_e} - \bar{v}_j \leq 0, j = 1, \dots, m \\ & 0 \leq z_{ij} \leq 1, i = 1, \dots, N_c \end{aligned} \quad (5)$$

where N is the number of all beam nodes' degrees of freedoms(DOFs). \bar{v}_j is the volume fraction of the j^{th} candidate material. \mathbf{z} , as the matrix of design variables, represents m density fields of the m candidate materials. \hat{z}_{ij} is the filtered matrix of design variables, defined as:

$$\hat{\mathbf{z}} = \mathbf{P} \mathbf{z} \quad (6)$$

where \mathbf{P} is the filter matrix, which is provided in section 3.4.

3.2 Material interpolation

In this work, the SIMP model [21] is adopted to penalize intermediate densities.

$$w_{ij} = \hat{z}_{ij}^p \quad (7)$$

where $p > 1$ is SIMP penalty parameter which pushes design variables toward zero and one.

The multi-material interpolation function for active materials is expressed as:

$$\begin{cases} E_i = \bar{E} + \sum_{j=1}^m w_{ij} \sum_{t=1}^m (1 - \gamma w_{it}) (E_j^0 - \bar{E}) \\ g_i = \varepsilon + (1 - \varepsilon) \sum_{j=1}^m w_{ij} \sum_{t=1}^m (1 - \gamma w_{it}) g_j^0 \end{cases} \quad (8)$$

where E_j^0 is the Young's modulus and g_j^0 is the deformation coefficient of the j^{th} candidate active material.

$0 \leq \gamma \leq 1$ is mixing penalty parameter. \bar{E} is the Young's modulus of the passive material. ε is a small number, which is used to define the deformation coefficient of the passive material.

3.3 Sensitivity Analysis

We solve the optimization problem formulated in Eq.(5) using a gradient-based optimization method. It requires sensitivity information of object function and volume constraints function.

The sensitivity of object function can be expressed via the chain rule:

$$\frac{\partial J}{\partial z_{ij}} = \frac{\partial J}{\partial \mathbf{U}} \frac{\partial \mathbf{U}}{\partial z_{ij}} \quad (9)$$

The term of $\frac{\partial J}{\partial \mathbf{U}}$ is derived as:

$$\frac{\partial J}{\partial \mathbf{U}} = \frac{2(\mathbf{U} - \mathbf{U}^*)^T}{N} \quad (10)$$

By differentiation of $\mathbf{KU} = \mathbf{F}$, the term $\frac{\partial \mathbf{U}}{\partial z_{ij}}$ can be

derived as follows:

$$\frac{\partial \mathbf{U}}{\partial z_{ij}} = \mathbf{K}^{-1} \left(\frac{\partial \mathbf{F}}{\partial z_{ij}} - \frac{\partial \mathbf{K}}{\partial z_{ij}} \mathbf{U} \right) \quad (11)$$

Substituting Eq.(10) and Eq.(11) into Eq.(9) results in,

$$\frac{\partial J}{\partial z_{ij}} = \frac{2(\mathbf{U} - \mathbf{U}^*)^T}{N} \mathbf{K}^{-1} \left(\frac{\partial \mathbf{F}}{\partial z_{ij}} - \frac{\partial \mathbf{K}}{\partial z_{ij}} \mathbf{U} \right) \quad (12)$$

In this work, the adjoint method is employed for sensitivity analysis. We define an adjoint vector as:

$$\boldsymbol{\xi}^T = \frac{2(\mathbf{U} - \mathbf{U}^*)^T}{N} \mathbf{K}^{-1} \quad (13)$$

where the adjoint vector $\boldsymbol{\xi}$ can be calculated from the following adjoint equation

$$\mathbf{K} \boldsymbol{\xi} = \frac{2(\mathbf{U} - \mathbf{U}^*)}{N} \quad (14)$$

By inserting the adjoint vector $\boldsymbol{\xi}$, Eq.(12) is expressed as:

$$\frac{\partial J}{\partial z_{ej}} = \boldsymbol{\xi}^T \left(\frac{\partial \mathbf{f}_e}{\partial w_{ij}} - \frac{\partial \mathbf{k}_e}{\partial w_{ij}} \mathbf{u}_e \right) \frac{\partial w_{ij}}{\partial z_{ij}} \quad (15)$$

where

$$\frac{\partial \mathbf{f}_e}{\partial w_{ij}} = \frac{\partial \mathbf{f}_e}{\partial \hat{E}_e} \frac{\partial \hat{E}_e}{\partial E_i} \frac{\partial E_i}{\partial w_{ij}} + \frac{\partial \mathbf{f}_e}{\partial \hat{g}_e} \frac{\partial \hat{g}_e}{\partial g_i} \frac{\partial g_i}{\partial w_{ij}} \quad (16)$$

The term $\frac{\partial \mathbf{f}_e}{\partial \hat{E}_e}$ and $\frac{\partial \mathbf{f}_e}{\partial \hat{g}_e}$ gives:

$$\begin{cases} \frac{\partial \mathbf{f}_e}{\partial \hat{E}_e} = A \hat{g}_e \mathbf{f}^0, \frac{\partial \mathbf{f}_e}{\partial \hat{g}_e} = A \hat{E}_e \mathbf{f}^0 \\ \mathbf{f}^0 = \mathbf{T}_e^T [-1 \ 0 \ 0 \ 1 \ 0 \ 0]^T \end{cases} \quad (17)$$

where \mathbf{T}_e^T is defined transform matrix, which transforms global coordinate system to local coordinate system.

The term $\frac{\partial \hat{E}_e}{\partial E_i}$ and $\frac{\partial \hat{g}_e}{\partial g_i}$ can be calculated by according to Eq.(1), respectively

$$\frac{\partial \hat{E}_e}{\partial E_i} = \begin{cases} \frac{2E_{e2}^2}{(E_{e1} + E_{e2})^2}, i = e1 \\ \frac{2E_{e1}^2}{(E_{e1} + E_{e2})^2}, i = e2 \\ 0, otherwise \end{cases} \quad (18)$$

$$\frac{\partial \hat{g}_e}{\partial g_i} = \begin{cases} \frac{2g_{e2}^2}{(g_{e1} + g_{e2})^2}, i = e1 \\ \frac{2g_{e1}^2}{(g_{e1} + g_{e2})^2}, i = e2 \\ 0, otherwise \end{cases} \quad (19)$$

From Eq.(8) the term $\frac{\partial E_i}{\partial w_{ij}}$ and $\frac{\partial g_i}{\partial w_{ij}}$ can be calculated by

$$\begin{cases} \frac{\partial E_i}{\partial w_{ij}} = \prod_{r=1, r \neq j}^m (1 - \gamma w_{ir}) (E_j^0 - \bar{E}) \\ \quad - \sum_{k=1, k \neq j}^m \gamma w_{ik} \prod_{t=1, t \neq j}^m (1 - \gamma w_{it}) (E_k^0 - \bar{E}) \\ \frac{\partial g_i}{\partial w_{ij}} = \prod_{r=1, r \neq j}^m (1 - \gamma w_{ir}) g_j^0 (1 - \varepsilon) \\ \quad - \sum_{k=1, k \neq j}^m \gamma w_{ik} \prod_{t=1, t \neq j}^m (1 - \gamma w_{it}) g_k^0 (1 - \varepsilon) \end{cases} \quad (20)$$

The term $\frac{\partial \mathbf{k}_e}{\partial w_{ij}}$ in Eq.(15) can be written as:

$$\frac{\partial \mathbf{k}_e}{\partial w_{ij}} = \frac{\partial \mathbf{k}_e}{\partial \hat{E}_e} \frac{\partial \hat{E}_e}{\partial E_i} \frac{\partial E_i}{\partial w_{ij}} \quad (21)$$

with

$$\frac{\partial \mathbf{k}_e}{\partial \hat{E}_e} = \mathbf{T}_e^T \bar{\mathbf{k}}_e^0 \mathbf{T}_e \quad (22)$$

where $\bar{\mathbf{k}}_e^0$ is the special case of $\bar{\mathbf{k}}_e$ in Eq.(2) when E is equal to 1.

From Eq.(7), The term $\frac{\partial w_{ij}}{\partial \hat{z}_{ij}}$ in Eq.(15) gives:

$$\frac{\partial w_{ij}}{\partial \hat{z}_{ij}} = p \hat{z}_{ij}^{p-1} \quad (23)$$

And from Eq.(6), The term $\frac{\partial \hat{z}_{ij}}{\partial z_{ij}}$ in Eq.(15) can be obtained:

$$\frac{\partial \hat{\mathbf{z}}_j}{\partial \mathbf{z}_j} = \mathbf{P}^T \quad (24)$$

where $\hat{\mathbf{z}}_j$ and \mathbf{z}_j are the j^{th} columns of $\hat{\mathbf{z}}$ and \mathbf{z} .

The derivatives of the volume constraints are:

$$\frac{\partial \varphi_j}{\partial z_{ij}} = \frac{\partial \varphi_j}{\partial \hat{z}_{ij}} \frac{\partial \hat{z}_{ij}}{\partial z_{ij}}, \frac{\partial \varphi_j}{\partial \hat{z}_{ij}} = \frac{1}{N_e} \quad (25)$$

3.4 Filtering and The ZPR design variable update

The density + ZPR filter [39] is applied to restrain checkerboard patterns as well as the islanding phenomenon. In terms of 4D printing, the checkerboard phenomenon means that there are regions where different materials are alternately distributed in voxels (resembling checkerboard patches). The islanding phenomenon means that a certain material voxel exists in isolation from other material regions. The material distribution caused by this phenomenon is not conducive to printing, and it further influences the shape matching and structure performance.

The filter matrix is obtained as follows [40][41]:

$$P_{ik} = \frac{w_{ik}}{\sum_{j=1}^{N_e} w_{ij}} \quad (26)$$

with

$$w_{ik} = \max \left(0, 1 - \frac{\|\mathbf{x}_i - \mathbf{x}_k\|_2}{R} \right)^q \quad (27)$$

where R is the filter radius. \mathbf{x}_i and \mathbf{x}_k are the centers of voxels i and k , respectively. $q = 2$ is the filter exponent.

The ZPR update [42] is a sequential linear programming technique. Linearized approximations to Eq.(5) are solved using Lagrangian duality at each optimization step. The ZPR method is very efficient in multiple volume constraints problem.

The ZPR design variable update is defined as:

$$z_{ij}^{new} = \begin{cases} \underline{z}_{ij}, B_{ij}^{\eta} \left(\sum_k P_{ik} z_{kj}^{old} \right) \leq \underline{z}_{ij} \\ \bar{z}_{ij}, B_{ij}^{\eta} \left(\sum_k P_{ik} z_{kj}^{old} \right) \geq \bar{z}_{ij} \\ B_{ij}^{\eta} \left(\sum_k P_{ik} z_{kj}^{old} \right), otherwise \end{cases} \quad (28)$$

where z_{ij}^{new} is the design variable for next iteration and z_{ij}^{old} is the design variable for current iteration. η is a damping parameter. \underline{z}_{ij} and \bar{z}_{ij} are the bounds which are given by the move limit δ :

$$\begin{cases} \underline{z}_{ij} = \max(0, z_{ij}^{old} - \delta) \\ \bar{z}_{ij} = \min(1, z_{ij}^{old} + \delta) \end{cases} \quad (29)$$

The term B_{ij} in Eq.(28) are:

$$B_{ij} = - \frac{\frac{\partial J}{\partial z_{ij}} \Big|_{z=z^{old}}}{\lambda_j \frac{\partial \varphi_j}{\partial z_{ij}} \Big|_{z=z^{old}}} \quad (30)$$

where λ_j is the Lagrange multiplier associated with the j^{th} constraint.

4. Numerical examples

To validate the effectiveness of the proposed approach, numerical examples considering two target shapes for the design problem of PAC are provided. The proposed method is applied for the design problem of a cantilever beam ($L = 70$ mm, $H = 10$ mm), whose design domain and boundary conditions are depicted in **Figure 5**. The left side of the design domain is fixed. The initial shape of the two numerical examples is the same as shown in **Figure 5(b)**.

The design domain is discretized into 140×20 voxels. Each voxel in the design domain is filled with passive material or different active materials to achieve cantilever beam deforms into a target shape from the initial shape. A volume constraint is considered to limit all the active materials to fill no more than 40% of the entire domain

volume. And the volume fraction of each active material is equal.

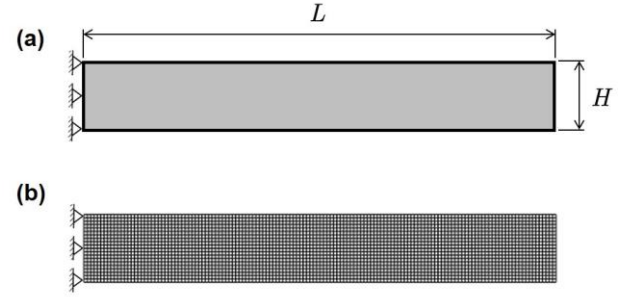


Figure 5. Schematic of the cantilever beam design problem (a)reference design domain (b) voxel mesh 140x20 voxels

A 4D printing inks have been proposed in Ref. [7]. The 4D printing inks are composed of elastomeric matrices with tunable cross-link density and anisotropic filler that enable precise control of their elastic modulus E and coefficient of thermal expansion α . The inks achieves that E ranges from 1.5×10^{-3} to 1.245 Mpa and α ranges from 32×10^{-6} to $229 \times 10^{-6} 1/^\circ\text{C}$. By using a temperature change $\Delta T = 250^\circ\text{C}$ as stimulus, the deformation coefficient g ranges from 0.008 to 0.0572.

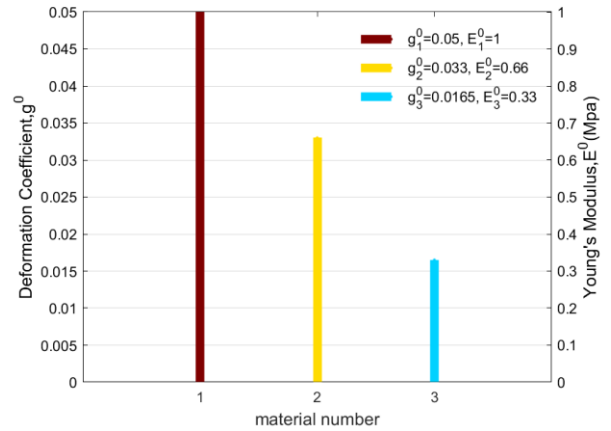


Figure 6. Coefficient of deformation and Young's modulus of the three candidate materials. Dark red, yellow and light blue represent different active materials

Based on the 4D printing inks, three hypothetical active materials and a passive material (as the non-active matrix) are used for candidate materials. The Young's modulus and deformation coefficient of the active materials are regularly spaced in the range $[0, 1]$ and $[0, 0.05]$, which are $E = [1, 0.66, 0.33]$ Mpa and $g = [0.05, 0.033, 0.165]$, respectively.

The Young's modulus of the passive material is $\bar{E} = 0.1$ Mpa. The deformation coefficient of the passive material is zero, which does not respond to the stimulus. As shown in **Figure**

6, each candidate material is assigned with a color used in the result visualization. In particular, the passive material is indicated in the color white.

For all cases, in order to avoid local optima and improve the convergence, SIMP penalty parameter p and mixing penalty parameter γ are respectively increased from 1 to 4 and 0 to 1 in the optimization process [43]. In the five continuation steps, the detailed values are $p = [1, 1.5, 2, 3, 4]$ and $\gamma = [0.2, 0.5, 1, 1, 1]$. The maximum number of iterations during each continuation step is set to 200. The final design of the previous continuation step is used as the initial design of the next continuation step. A constant filter radius of $R = 1.5$ mm is used. The move limit δ used in the ZPR update is 0.01. And the damping parameter of the ZPR update is chosen as $\eta = 0.5$. In the optimization process of each continuation step, the convergence criteria is either the maximum number of iterations or relative change of objective function in two successive iterations less than 10^{-5} .

4.1 Parabolic target shape

The first example is the parabolic target shape, whose voxelized object is depicted in **Figure 8**. The maximum deflection of the parabolic target shape is 8 mm and the

maximum twist angle of the control structure is 13° . The last two active materials (yellow and light blue) plotted in **Figure 6** are selected as the candidate materials in this case ($E = [0.66, 0.33]$, $g = [0.033, 0.0165]$).

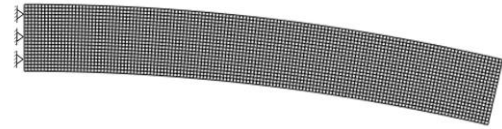


Figure 8. Parabolic target shape

As described in the above section, the SIMP penalty parameter p and the mixing penalty parameter γ in the material interpolation function are gradually increased to achieve the required penalization on intermediate densities as the optimization progresses. The initial designs of four continuation steps are adopted to show the evolutionary history of the material distribution and the corresponding shape matching during the optimization process. The point cloud composed of all the voxels' vertices is used to describe the geometry shape including achieved shape and target shape. The color of each voxel is the weighted average of the design variables and the corresponding colors of candidate

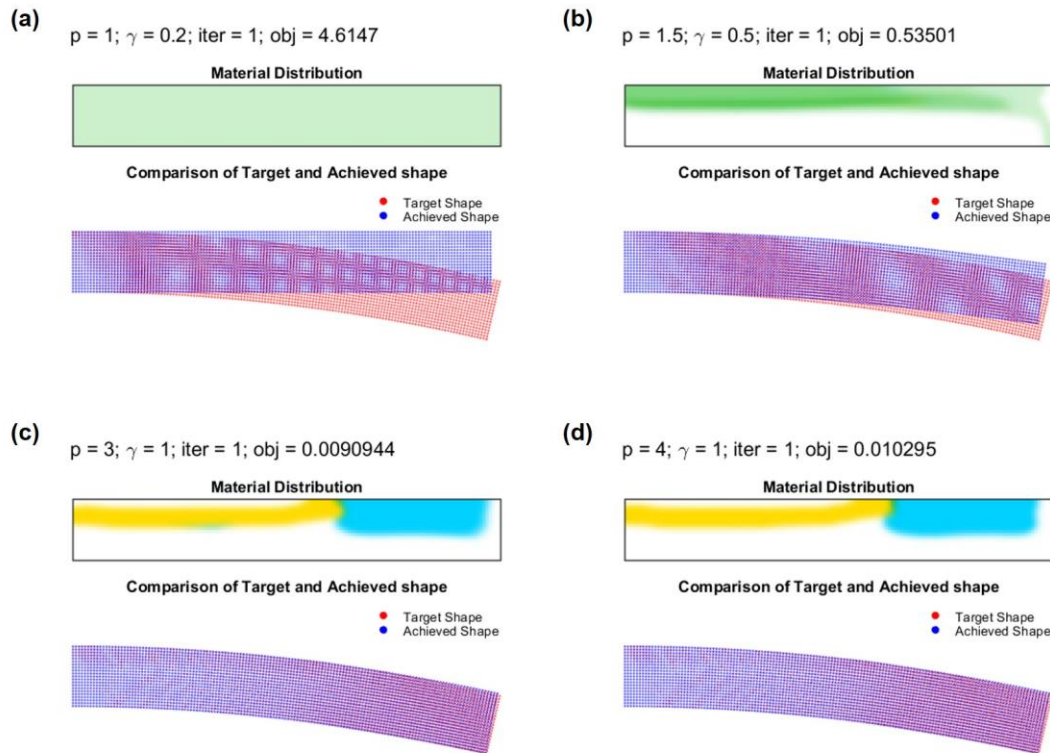


Figure 7. Evolution history of material distribution and achieved shape at the initial designs of four continuation steps for parabolic target shape (a) $p = 1, \gamma = 0.2$ (b) $p = 1.5, \gamma = 0.5$ (c) $p = 3, \gamma = 1$ (d) $p = 4, \gamma = 1$

materials. The initial guess of design variables is chosen as $z_{ej} = 0.4/2$, as shown in **Figure 7(a)**, which means that the chance of each candidate material is determined by its volume fraction. The objective function is the largest at the initial guess, which means that the mismatch between achieved shape and target shape is the largest. In **Figure 7(b)**, the material distribution is not only the final design of the first continuation step ($p = 1$, $\gamma = 0.2$), but also the initial design of the second continuation step ($p = 1.5$, $\gamma = 0.5$). It can be found that the distribution trend of passive material and active materials is beginning to emerge and material mixing is favorable. As the mixing penalty parameter γ is increased toward 1, material mixing is increasingly penalized in **Figure 7(c)**. As illustrated in **Figure 7(d)**, the mixed voxels in the yellow regions almost disappear by increasing the SIMP penalty parameter p to 4.

The final material distribution is presented in the upper part of **Figure 9**, where the objective function value is $J = 0.0086 \text{ mm}^2$ and the volume fraction of each active material is 0.2. It is noted that no checkerboard patterns as well as the islanding phenomenon happens with the proposed method. It can be found that there are only a very small regions of mixing that arise at the interfaces between materials due to the density filter. From the point cloud comparison in the lower part of **Figure 9**, the largest mismatch between achieved shape and target shape is present at the free end of the cantilever beam. But overall, the achieved shape is very close to the target shape.

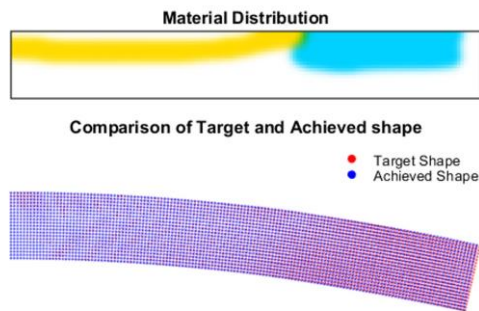


Figure 9. Final material distribution and shape comparison of parabolic target shape

4.2 Sinusoidal target shape

As a second example, the sinusoidal target shape is considered. Its voxelized object is plotted in **Figure 10**. The maximum deflection of the parabolic target shape is 12 mm and the maximum twist angle of the control structure is 13° . Compared with the parabolic target shape in the first

example, the sinusoidal target shape is relatively more complex. Therefore, all the three active materials illustrated in **Figure 6** are chosen as candidate materials in this case.

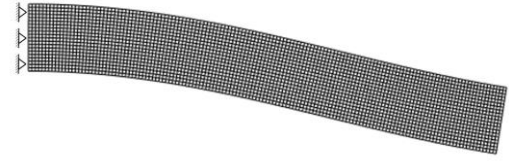


Figure 10. Sinusoidal target shape

As illustrated in **Figure 12(a)**, there are three candidate active materials in this example, the initial guess of design variables is therefore set to $z_{ej} = 0.4/3$, and the cantilever beam is almost in an undeformed state. The initial designs and the corresponding shape matching of four continuation steps are observed. After the first continuation step, active materials accumulate in some regions and material mixing occupies most regions of the design domain as shown in **Figure 12(b)**. The mismatch between achieved shape and target shape rapidly decreases in the initial continuation step. As γ is increased toward 1, a relatively clear material distribution appears after the third continuation step ($p = 2$, $\gamma = 1$) depicted in **Figure 12(c)**. It can be seen in the lower part of **Figure 12(c)** that the achieved shape is quite close to the target shape. But there are some intermediate densities near the dark red region. As illustrated in **Figure 12(d)**, both material mixing and intermediate densities are penalized after the fourth continuation step ($p = 3$, $\gamma = 1$).

As visualized in the upper part of **Figure 11**, checkerboard patterns and the islanding phenomenon are effectively suppressed in the final material distribution. The objective function converges at 0.0476 mm^2 and the volume fraction of each active material is equal to 0.133 in the final design. The achieved shape is smooth and regular plotted in the lower part of **Figure 11**. It is worthy to observe that the material distribution becomes less intuitive in the example of sinusoidal target shape, which highlights the advantages of the proposed optimization method. Very small regions of mixing remain on the border at the interfaces between materials which is attributed to the density filter. As shown in the point cloud comparison in the lower part of **Figure 11**, the largest mismatch between achieved shape and target shape occurs at the free end and the upper middle of the cantilever beam. However, the achieved shape is close enough to the target shape.

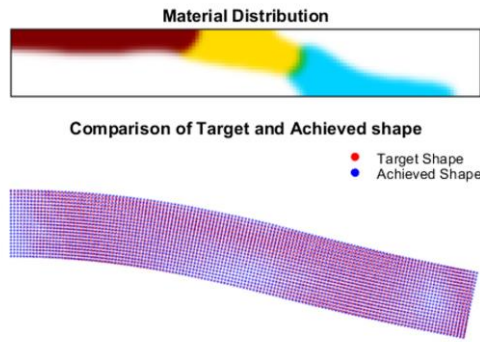


Figure 11. Final material distribution and shape comparison of sinusoidal target shape

5. Discussion

The inverse mechanics problem for the design of PACs towards 4D printing was transformed into a volume-constrained, shape-matching, error-minimization problem with multiple materials. The proposed method focused on finding the best distribution of the various active materials and a passive material such that the PAC assumed a target shape. The examples included parabolic and sinusoidal target shapes. The numerical results illustrate the clear descriptions of the material distributions and a smooth target shape

corresponding to the final design, as presented in **Figure 9** and **Figure 11**.

In order to visualize the convergence histories along the optimization process in each continuation step more clearly, the objective functions were plotted with Logarithmic coordinates. The initial objective function of the sinusoidal target shape had a value of 14.8917 mm^2 , which is three times as high as that of the parabolic target shape (4.6147 mm^2). Further indicating that the sinusoidal target is more complex than the parabolic target. As shown in **Figure 13**, an abrupt changed objective value at the beginning of each successive step was obtained since the penalty parameters were gradually increased, and the amplitudes of abrupt changes also decreased. The objective function value decreased steadily in each continuation step and finally converged to the optimal value near zero. As depicted in **Figure 13(a)**, the proposed method required 361 iterations to satisfy the convergence criterion for a parabolic target shape. In **Figure 13(b)**, the entire optimization process for a sinusoidal target shape was completed in 524 iterations.

The method had several advantages. One was that the filter was excellent for eliminating checkerboard patterns and the islanding phenomenon. Thus, the final design was amenable for multi-material 3D printing and for the smooth deformed shape, especially referring to very small voxel sizes. The second advantage was that the multi-material

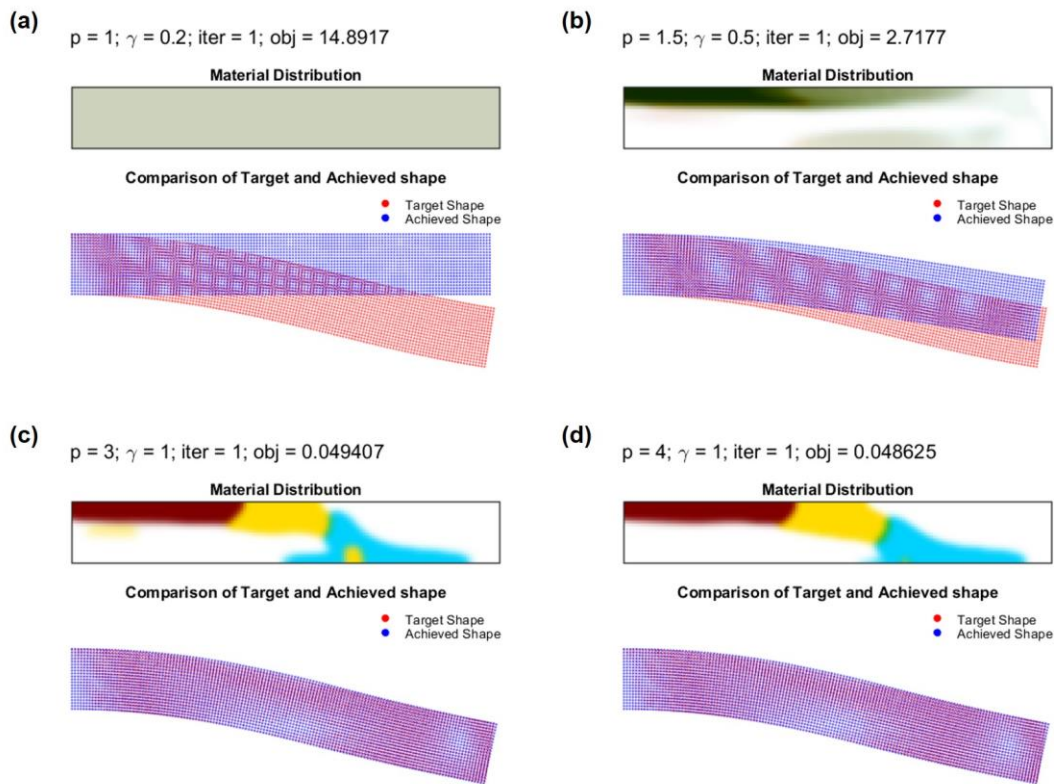


Figure 12. Evolution history of material distribution and achieved shape at the initial designs of four continuation steps for sinusoidal target shape (a) $p = 1, \gamma = 0.2$ (b) $p = 1.5, \gamma = 0.5$ (c) $p = 3, \gamma = 1$ (d) $p = 4, \gamma = 1$

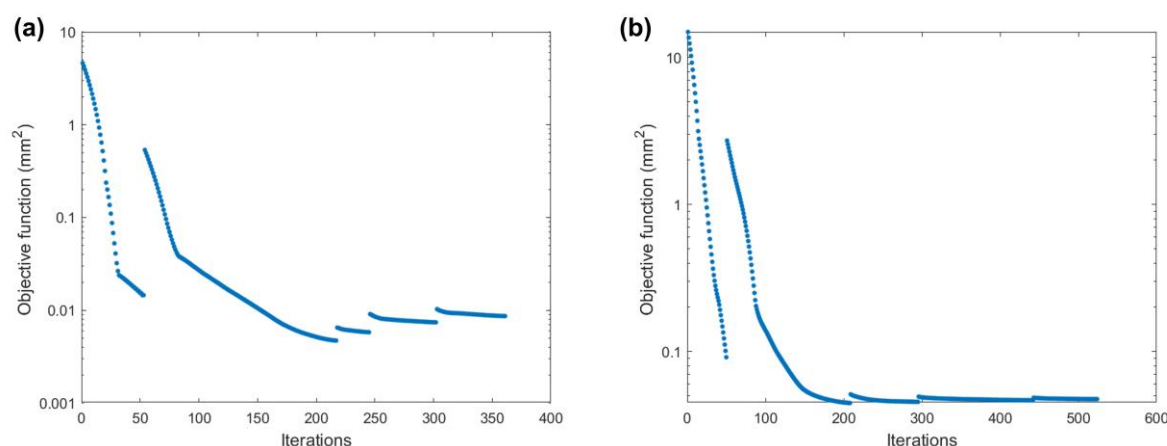


Figure 13. Convergence histories along the optimization process (a) parabolic target shape (b) sinusoidal target shape. Logarithmic scale has been chosen for clear depiction of objective function convergence.

interpolation scheme for active materials matched the target shapes with high accuracy. Finer voxelization was required to ensure high-accuracy matching of the shape when a more complex target shape was considered. However, increasing the number of voxels can result in very large computational costs for the objective function when using finite-element methods to solve the PAC deformation for a given material distribution. Hence, the response behavior of the deformation was modeled via continuum mechanics model. In this scheme, the deformations of the optimized designs were calculated by deformations of control structures that used beams to connect voxel centers. The continuum mechanics model enables the low computational costs for the objective function, which is the third advantage. Further studies will focus on an extension to 3D cases. In addition, large deformations and a complex thermomechanical constitutive model to accurately predict the response of PACs will be conducted.

6. Conclusion

Multi-material topology optimization for the design of PACs was proposed to achieve target-shape-matching in 4D printing. A multi-material interpolation equation for active materials was developed to model material distributions as continuous variables. Updating of material distributions was based on sensitivity information, and the ZPR design-variable update scheme was implemented to minimize the objective function. High-accuracy matching between the target shapes and the final shapes was achieved within reasonable errors. Several numerical examples were demonstrated in which different target shapes and different amounts of active materials were examined to verify the feasibility and effectiveness of the proposed method. From the numerical results, the material distributions were less intuitive as the complexity of the target shape increased. This highlighted the advantages of the optimization method.

Acknowledgements

This work is supported by the National Natural Science Foundation of China (52003291).

References

- [1] Wu J, Yuan C, Ding Z, Isakov M, Mao Y, Wang T, Dunn M L and Qi H J 2016 Multi-shape active composites by 3D printing of digital shape memory polymers *Sci. Rep.* **6** 24224
- [2] Hager M D, Bode S, Weber C and Schubert U S 2015 Shape memory polymers: Past, present and future developments *Prog. Polym. Sci.* **49–50** 3–33
- [3] Wang S, Decker M, Henann D L and Chester S A 2016 Modeling of dielectric viscoelastomers with application to electromechanical instabilities *J. Mech. Phys. Solids* **95** 213–29
- [4] Yuan C, Roach D J, Dunn C K, Mu Q, Kuang X, Yakacki C M, Wang T J, Yu K and Qi H J 2017 3D printed reversible shape changing soft actuators assisted by liquid crystal elastomers *Soft Matter* **13** 5558–68
- [5] Roach D J, Kuang X, Yuan C, Chen K and Qi H J 2018 Novel ink for ambient condition printing of liquid crystal elastomers for 4D printing *Smart Mater. Struct.* **27** 125011
- [6] Wang Q, Tian X, Huang L, Li D, Malakhov A V. and Polilov A N 2018 Programmable morphing composites with embedded continuous fibers by 4D printing *Mater. Des.* **155** 404–13
- [7] Boley J W, Van Rees W M, Lissandrello C, Horenstein M N, Truby R L, Kotikian A, Lewis J A and Mahadevan L 2019 Shape-shifting structured lattices via multimaterial 4D printing *Proc. Natl. Acad. Sci. U. S. A.* **116** 20856–62
- [8] Huang T Y, Huang H W, Jin D D, Chen Q Y, Huang J Y, Zhang L and Duan H L 2020 Four-dimensional micro-building blocks *Sci. Adv.* **6** eaav8219
- [9] De Haan L T, Verjans J M N, Broer D J, Bastiaansen C W M and Schenning A P H J 2014 Humidity-responsive liquid crystalline polymer actuators with an asymmetry in the molecular trigger that bend, fold, and curl *J. Am. Chem. Soc.* **136** 10585–8
- [10] Diguett G, Beaunon E and Cavallé J Y 2010 Shape effect in the magnetostriction of ferromagnetic composite *J. Magn. Magn. Mater.* **322** 3337–41

- [11] Elhajjar R, Law C-T and Pegoretti A 2018 Magnetostrictive polymer composites: Recent advances in materials, structures and properties *Prog. Mater. Sci.* **97** 204–29
- [12] Miriyev A, Stack K and Lipson H 2017 Soft material for soft actuators *Nat. Commun.* **8** 596
- [13] Ali M H, Abilgazyev A and Adair D 2019 4D printing: a critical review of current developments, and future prospects *Int. J. Adv. Manuf. Technol.* **105** 701–17
- [14] Momeni F, M.Mehdi Hassani, N S, Liu X and Ni J 2017 A review of 4D printing *Mater. Des.* **122** 42–79
- [15] Maute K, Tkachuk A, Wu J, Qi H, Ding Z and Dunn M 2015 Level Set Topology Optimization of Printed Active Composites *J. Mech. Des.* **137** 111402
- [16] Ge Q, Qi H J and Dunn M L 2013 Active materials by four-dimension printing *Appl. Phys. Lett.* **103** 131901
- [17] Ge Q, Sakhaei A H, Lee H, Dunn C K, Fang N X and Dunn M L 2016 Multimaterial 4D Printing with Tailorable Shape Memory Polymers *Sci. Rep.* **6** 31110
- [18] Hamel C M, Roach D J, Long K N, Demoly F, Dunn M L and Qi H J 2019 Machine-learning based design of active composite structures for 4D printing *Smart Mater. Struct.* **28** 065005
- [19] Sossou G, Demoly F, Belkebir H, Qi H J, Gomes S and Montavon G 2019 Design for 4D printing: Modeling and computation of smart materials distributions *Mater. Des.* **181** 108074
- [20] Bendsøe M P and Sigmund O 1999 Material interpolation schemes in topology optimization *Arch. Appl. Mech.* **69** 635–54
- [21] Bendsøe M P 1989 Optimal shape design as a material distribution problem *Struct. Optim.* **1** 193–202
- [22] Wang M Y, Wang X and Guo D 2003 A level set method for structural topology optimization *Comput. Methods Appl. Mech. Eng.* **192** 227–46
- [23] Xie Y M and Steven G P 1993 A simple evolutionary procedure for structural optimization *Comput. Struct.* **49** 885–96
- [24] Huang X, Xie Y M and Burry M C 2007 A new algorithm for bi-directional evolutionary structural optimization *JSME Int. Journal, Ser. C Mech. Syst. Mach. Elem. Manuf.* **49** 1091–9
- [25] Xue R, Liu C, Zhang W, Zhu Y, Tang S, Du Z and Guo X 2019 Explicit structural topology optimization under finite deformation via Moving Morphable Void (MMV) approach *Comput. Methods Appl. Mech. Eng.* **344** 798–818
- [26] Zhang W, Yuan J, Zhang J and Guo X 2016 A new topology optimization approach based on Moving Morphable Components (MMC) and the ersatz material model *Struct. Multidiscip. Optim.* **53** 1243–60
- [27] Bourdin B and Chambolle A 2003 Design-dependent loads in topology optimization *ESAIM - Control. Optim. Calc. Var.* **9** 247–73
- [28] Dedè L, Borden M J and Hughes T J R 2012 Isogeometric Analysis for Topology Optimization with a Phase Field Model *Arch. Comput. Methods Eng.* **19** 427–65
- [29] Sui Y and Peng X 2006 ICM method with objective function transformed by variable discrete condition for continuum structure *Acta Mech. Sin. Xuebao* **22** 68–75
- [30] Peng X and Sui Y 2018 ICM method for fail-safe topology optimization of continuum structures *Lixue Xuebao/Chinese J. Theor. Appl. Mech.* **50** 611–21
- [31] Cai S and Zhang W 2020 An adaptive bubble method for structural shape and topology optimization *Comput. Methods Appl. Mech. Eng.* **360** 112778
- [32] Geiss M J, Boddeti N, Weeger O, Maute K and Dunn M L 2019 Combined Level-Set-XFEM-Density Topology Optimization of Four-Dimensional Printed Structures Undergoing Large Deformation *J. Mech. Des. Trans. ASME* **141** 051405
- [33] Zolfagharian A, Denk M, Bodaghi M, Kouzani A and Kaynak A 2020 Topology-Optimized 4D Printing of a Soft Actuator *Acta Mech. Solida Sin.* **33** 418–30
- [34] Zolfagharian A, Denk M, Kouzani A Z, Bodaghi M, Nahavandi S and Kaynak A 2020 Effects of Topology Optimization in Multimaterial 3D Bioprinting of Soft Actuators. *Int. J. bioprinting* **6** 260
- [35] Zhang H, Kumar A S, Fuh J Y H and Wang M Y 2018 Topology optimized design, fabrication and evaluation of a multimaterial soft gripper 2018 *IEEE International Conference on Soft Robotics (RoboSoft)* pp 424–30
- [36] Sossou G, Demoly F, Belkebir H, Qi H J, Gomes S and Montavon G 2019 Design for 4D printing: A voxel-based modeling and simulation of smart materials *Mater. Des.* **175** 107798
- [37] Okereke M and Keates S 2018 Direct Stiffness Method *Finite Element Applications: A Practical Guide to the FEM Process* (Cham: Springer International Publishing) pp 47–106
- [38] Keith D. Hjelmstad 2005 *The Linear Theory of Beams Fundamentals of Structural Mechanics* (Boston, MA: Springer US) pp 241–91
- [39] Sanders E D, Aguiló M A and Paulino G H 2018 Multi-material continuum topology optimization with arbitrary volume and mass constraints *Comput. Methods Appl. Mech. Eng.* **340** 798–823
- [40] Talischi C, Paulino G H, Pereira A and Menezes I F M 2012 PolyTop: a Matlab implementation of a general topology optimization framework using unstructured polygonal finite element meshes *Struct. Multidiscip. Optim.* **45** 329–57
- [41] Giraldo-Londoño O and Paulino G H 2021 PolyStress: a Matlab implementation for local stress-constrained topology optimization using the augmented Lagrangian method *Struct. Multidiscip. Optim.* **63** 2065–97
- [42] Zhang X S, Paulino G H and Ramos A S 2018 Multi-material topology optimization with multiple volume constraints: a general approach applied to ground structures with material nonlinearity *Struct. Multidiscip. Optim.* **57** 161–82
- [43] Sanders E D, Pereira A, Aguiló M A and Paulino G H 2018 PolyMat: an efficient Matlab code for multi-material topology optimization *Struct. Multidiscip. Optim.* **58** 2727–59